Journal of Physics and Chemistry of Solids 161 (2022) 110420

Contents lists available at ScienceDirect

Journal of Physics and Chemistry of Solids

journal homepage: www.elsevier.com/locate/jpcs

Colloidal processing of thulium-yttria microceramics

S.C. Santos *, O. Rodrigues Jr., L.L. Campos

Instituto de Pesquisas Energéticas e Nucleares IPEN-CNEN, Av. Prof. Lineu Prestes 2242, Cidade Universitaria - CEP, 05508-000, São Paulo, Brasil

ARTICLE INFO

Keywords:
Yttria
Thulium oxide
Rare earths
Bio-prototyping
Dosimetry
Ceramic processing

ABSTRACT

The development of new dosimetric materials is essential for the safe and effective use of nuclear technology. In the present study, an eco-friendly bio-prototyping approach was developed for preparing thulium-yttria microceramics with potential applications in radiation dosimetry. Micro-powder compacts were obtained by casting colloidal thulium-yttria suspensions prepared with 20 vol% particles in thin-walled tube templates. Samples were sintered at 1600 °C for 2 h under the environmental pressure and atmosphere to obtain thulium-yttria microceramics with dimensions of 3.33 ± 0.01 mm × 2.27 ± 0.01 mm (height × diameter), as well as a cubic C-type structure, pycnometric density of 4.79 g cm^{-3} (95.61% theoretical density), and surface microstructure comprising hexagon-like grains bonded at the boundaries. The use of thulium as an activator of yttria greatly improved the electron paramagnetic resonance (EPR) response of the microceramics, where the main EPR peak (p_1) was recorded at 351.24 mT and the g factor was 2.0046. The innovative findings obtained in this study may facilitate the production of new solid state dosimeters.

1. Introduction

The use of radiation in various areas such as medicine [1], industry [2], energy [3], and food [4] has provided great benefits to society. However, nuclear technology requires advanced materials to ensure that the application of radiation in the long term is high quality, safe, and effective. Dosimetric materials can absorb radiation energy and release it in the form of visible light when optically or thermally stimulated [5–7].

Magnesium, titanium co-doped lithium fluoride (LiF:Mg, Ti) [8], magnesium, copper, phosphor tri-doped lithium fluoride (LiF:Mg, Cu, P) [9], and manganese doped lithium tetraborate ($Li_2B_4O_7$:Mn) [10] are commonly used in clinical dosimetry due to their tissue equivalence. Despite their higher atomic effective number, dysprosium doped calcium sulfate ($CaSO_4$:Dy) [11], carbon doped aluminium oxide (Al_2O_3:C) [12], and dysprosium doped calcium fluoride (CaF_2:Dy) [13] have been used widely in clinical, environmental, industrial, and personal dosimetry because of their high dose sensitivity.

A material that is available in the form of a free powder is not very useful for dosimetry because free powders are difficult to manipulate during routine work. Therefore, a process is required to consolidate powders into a compacted body. Bio-prototyping is an eco-friendly process that allows the shaping of advanced materials by using renewable templates and colloidal suspensions. The inter-particle forces are controlled in order to consolidate the particles and obtain a powder compact. Furthermore, thermal treatment is performed to enhance the mechanical strength of compacts and form the microstructure, which is effective for improving the characteristics of the material and its components. Previously, our research group investigated bio-prototyping for materials such as biomorphic dysprosium-yttrium disilicate [14], yttria nettings [15], yttrium disilicate micro-cellular burners [16], and europium-yttria rods [17]. These previous studies confirmed that bio-prototyping is a useful process for producing advanced materials.

Nuclear technology demands the continuous development of advanced materials in order to ensure that the use of radiation is totally safe. Yttria (Y_2O_3) belongs to the rare earth (RE) group and its unique properties have facilitated a broad range of applications in biomaterials [18], superconductors [19], scintillators [20], capacitors [21], and catalysis [22]. Moreover, yttria exhibits lattice characteristics that allow the insertion of other RE ions into its structure (doping). According to the type of RE ion, valence state, content, and position in the host lattice, the solid state characteristics of yttria can be greatly enhanced [23–28]. Oliveira et al. [29] improved the up-conversion luminescence of highly crystalline (Eu^{3+}, Er^{3+}, Yb^{3+}):Y_2O_3 nanoparticles by using sorbitol as a polymerizing agent. Yuan et al. [30] significantly enhanced the luminescence of Eu^{3+}:Y_2O_3/Y_2O_2S nanocomposites excited at 338 nm by reducing Eu^{3+}:Y_2O_3 nanoparticles. Huerta et al. [31] reported that the effective luminescence of (Er^{3+}, Yb^{3+}):Y_2O_3 nanoparticles was achieved

* Corresponding author.
E-mail addresses: silas.cardoso@alumni.usp.br (S.C. Santos), rodrijr@ipen.br (O. Rodrigues), lcrodri@ipen.br (L.L. Campos).

https://doi.org/10.1016/j.jpcs.2021.110420
Received 11 April 2021; Received in revised form 1 October 2021; Accepted 4 October 2021
Available online 6 October 2021
0022-3697/© 2021 Elsevier Ltd. All rights reserved.

through Er^{3+} to Yb^{3+} energy transfer. Considering the special features and broad applicability of RE oxides, members of this group of materials are classified as critical materials in the European Union [32] and United States of America [33].

In the present study, we extended our recent research [34] where we developed an alternative hydrothermal synthesis method to obtain thulium-yttria nanoparticles with controlled powder characteristics and electron paramagnetic resonance (EPR) response. Doping yttria with thulium improves the EPR response of yttria as a function of the radiation dose. As described in our recent study, thulium-yttria nanoparticles prepared with 0.01 at% Tm (atomic percentage, at%) exhibited a cubic C-type structure, mean particle diameter of around 96 nm, and the most remarkable EPR response among all of the compositions obtained. This response was related to the Tm content, where the insertion of low concentrations of Tm led to the formation of substantial crystal defects, which could trap more of the unpaired electrons formed during the irradiation process.

In the present study, we contributed further to the development of a promising solid state dosimeter by using an eco-friendly bio-prototyping approach to prepared thulium-yttria microceramics with potential applications in radiation dosimetry.

2. Experimental

2.1. Powder synthesis and characterization

Thulium-yttria powders (Tm:Y_2O_3) prepared with 0.1 at% Tm were synthesized using an eco-friendly hydrothermal process as described previously [35].

The as-synthesized Tm:Y_2O_3 powders were characterized by photon correlation spectroscopy (Litesizer500, Anton Paar) according to the following parameters: diluted aqueous suspensions (0.05%vol), equilibration time = 10 s, number of runs = 5, evaluation time = 20 s, and temperature = 25 °C. We also conducted helium pycnometry (Pycnometer Micrometrics 1330), X-ray diffraction (XRD, Rigaku Multiflex, Japan) with an angular range (2θ) from 15° to 70° and scanning at 0.5° min^{-1} with a Kα source, and scanning electron microscopy (SEM, INCAx-act, Oxford Instruments).

2.2. Colloidal stability based on zeta potential (ζ) determination

The stability of the Tm:Y_2O_3 particles in aqueous solvent was evaluated based on electrophoretic mobility measurements (μe) obtained at room temperature (20 °C), before calculating the zeta potential (ζ) considering the Smoluchowski model given in Eq. (1) [36,37]. The stability of the particles was evaluated using stock suspensions containing 0.5 g L^{-1} of particles, 1 mM NaCl (58.54 g mol^{-1}, Merck) as the electrolyte, and HCl and KOH solutions.

$$\zeta = \left(\frac{\mu_e \cdot \eta}{\varepsilon}\right)[mV] \quad (1)$$

In Eq. (1), ϵ is permittivity of the liquid (J V^{-2} m), η is the viscosity of the liquid (cP), and μe is the electrophoretic mobility of the particles (μ s^{-1} V^{-1} cm).

2.3. Formulation of colloidal suspensions

Ceramic suspensions containing 20 vol% Tm:Y_2O_3 particles were prepared with tetramethylammonium hydroxide (30 wt%, Sigma Aldrich) and 0.2 wt% corn starch as a binder (CS, Maizena), which were subjected to ball milling for 24 h using alumina spheres ($Ø_{spheres}$ = 10 mm).

2.4. Preparation of thulium-yttria microceramics by bio-prototyping

Thulium-yttria microceramics were produced using an eco-friendly bio-prototyping method (Fig. 1), where ceramic suspensions were shaped using renewable templates to obtain almost net-shaped components for advanced application.

The shaped compacts were dried in an air atmosphere at the environmental temperature for 24 h. The powder compacts were then sintered at 1600 °C for 2 h in an air atmosphere and at a heating rate of 5 °C min^{-1}.

2.5. Microstructural evaluation of the microceramics

The as-sintered Tm:Y_2O_3 microceramics were characterized using optical microscopy (OM, Nikon SMZ1270), SEM (TM 3000, Hitachi; INCAx-act, Oxford Instruments), XRD (Rigaku Multiflex) at a scanning rate of 0.5°min^{-1} from 15 to 70° (2θ) with Cu-Kα radiation, and helium pycnometry (Pycnometer Micrometrics 1330).

2.6. EPR responses of the microceramics

The paramagnetic responses of the thulium-yttria microceramics were evaluated by EPR using an X-band EPR spectrometer (Bruker EMX PLUS) at room temperature and atmosphere. EPR spectra were recorded for the samples using the following parameters: field modulation frequency = 100 kHz, microwave power = 2.5 mW, center field = 300 mT, sweep width = 300 mT, modulation amplitude = 0.4 mT, time constant = 0.01 ms, with 10 scans, temperature of 20 °C, environmental atmosphere under controlled humidity, and 2,2-diphenyl-1-picrylhydrazyl (Bruker) was the EPR reference.

3. Results and discussion

The XRD curve obtained for thulium-yttria powders prepared using a relatively low temperature hydrothermal method [35], followed by annealing at 1100 °C for 2 h in an air atmosphere is illustrated in Fig. 2a. The as-synthesized powders had a cubic C-type structure and a high intensity diffraction peak was recorded at 29.5°, which indicated the (222) plane and corresponded to powder diffraction file (PDF) 25-100. Considering the crystallographic characteristics of yttria, the cubic C-type structure belongs to the Ia^3 space group, with 16 formula units per unit cell, six-coordination number (N), two points symmetry (S_6, C_{3i}), and C_2 [38]. Moreover, yttria has many oxygen vacancies [39,40] that allow the incorporation of other RE ions into the lattice, such as Er^{3+} [41], Dy^{3+} [42], and Yb^{3+} [43]. In addition, no secondary diffraction peaks were observed (Fig. 2a), thereby confirming that the proposed synthesis method was satisfactory for incorporating thulium ions into the yttria lattice.

Based on the phase diagram for RE oxides illustrated in Fig. 2b, REs can exhibit one of the following crystal forms according to the annealing temperature: A, B, C, X, or H. The A-type form (La, Ce, Pr, Nd, and Pm) has a characteristic hexagonal structure, with space group $P_{32/m}$, one unit formula per unit cell, and a metal atom in seven coordination. The B-type form (Pm, Sm, Eu, Gd, Tb, Dy, Ho, Er, Tm, Yb, and Lu) has a monoclinic structure, space group $C_{2/m}$, six formula units per unit cell, and metal atoms in six-seven coordination [44,45]. The C-type form (from La to Lu) is the most favorable for consolidation among all five forms, even under high temperatures. At 1000 °C, members of the RE group from Eu to Lu, including Sc and Y, tend to have the C-type form. Moreover, the C-type form has a characteristic cubic structure, space group I_{a3}, 32 metal atoms per unit cell, 48 oxygens per unit cell, and metal atoms in six-coordination [46]. The last two forms comprising H and X are just below the melting point (2400 °C). The H-type form exhibits has a hexagonal structure similar to A-type and space group $P_{63/mmc}$, whereas the X-type form has a cubic structure and space group I_{m3m} [47–49].

As described above, the cubic C-type is the most favorable form in which REs crystallize. However, REs undergo phase transformations at lower temperatures and under higher pressure. According to Hoestra

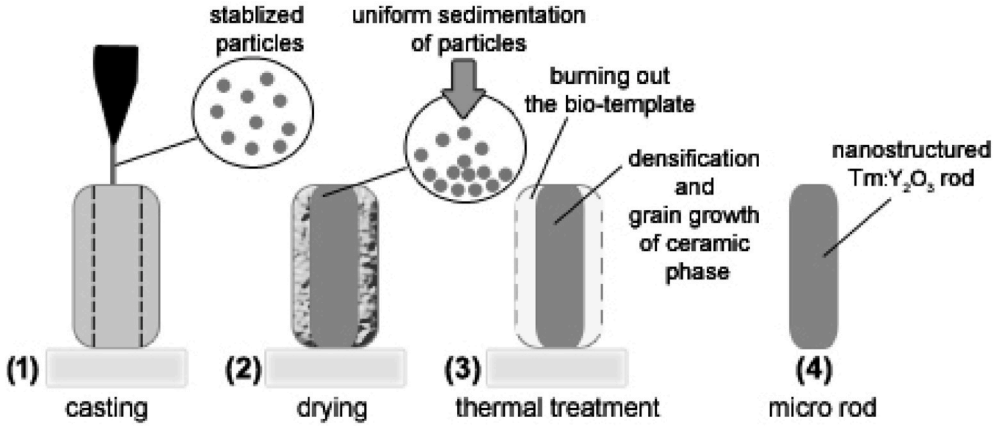

Fig. 1. Formation of thulium-yttria microceramics by bio-prototyping.

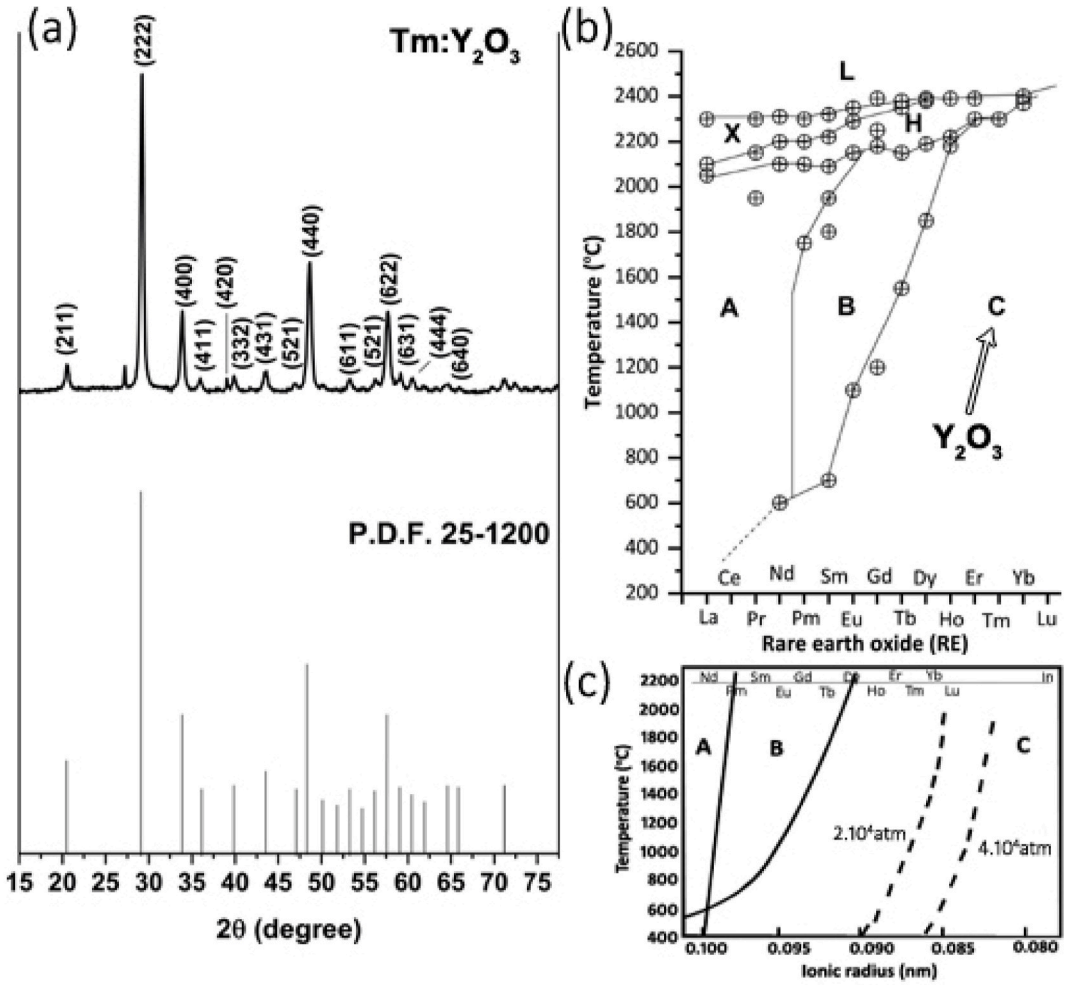

Fig. 2. (a) XRD curve obtained for thulium-yttria powders produced using the hydrothermal method, followed by annealing at 1100 °C for 2 h in an air atmosphere. Phase diagrams of RE polymorphs as functions (b) of temperature, and (c) temperature and pressure.

et al. [50], REs tend to stabilize as the A-type rather than the B-type and C-type under high pressure, and the B-type rather than the C-type. Moreover, Hoekstra et al. [51] observed that the phase transformations of REs can be reversible when samples are thermally treated under higher temperatures for a few hours after reducing the pressure. As illustrated in Fig. 2c, the equilibrium temperature phase from 1 atm to 2.10^4 atm is larger than that from 2.10^4 atm to 4.10^4 atm, and it was observed that the conversion of the structure of yttria from the B-type to C-type occurred after thermal treatment at 900 °C in the air under ambient pressure for several hours. Other studies have reported yttria polymorphisms such as C→B [51], C→fluorite [52], and C→A [53].

Particle size is the most important parameter in powder processing. In general, a powder comprises many particles with distinct sizes. Thus, evaluating the particle size distribution is important for obtaining the mean particle size (d_{50}), as well as the minor and higher diameter size distributions denoted as d_{10} and d_{90}, respectively. The mean particle size

distribution for the thulium-yttria powders is illustrated in Fig. 3a. The proposed synthesis method resulted in the formation of fine particles with a mean diameter size (d_{50}) around 98.8 nm. The other particle size distribution parameters indicated that the thulium-yttria powders were characterized by a narrow particle size distribution, span, where the difference between the d_{90} and d_{10} distributions was 59.9 nm, i.e., the relative span, and thus the ratio between the span and d_{50} was 0.6, and the polydispersity index was 0.2. In previous studies of the synthesis of RE-based materials, our research group reported the formation of the following materials: yttrium disilicate (d_{50} = 185 nm) [16], dyprosium-yttrium disilicate (d_{50} = 242 nm) [14], and europium-yttria (d_{50} = 576 nm) [54].

The morphology of particles is a fundamental parameter of a powder in the same manner as the particle size. As illustrated in Fig. 3b, the thulium-yttria powders comprised agglomerates of rounded particles. Nanoparticles are characterized by a high surface area and low mass/size ratio, so the attractive forces are highly effective at promoting the agglomeration of particles. Fortunately, these agglomerates are easily broken by crushing. Yu et al. [55] reported that the synthesis conditions led to changes in the morphology of Dy^{3+}/Eu^{3+} co-doped $Ca_3(PO_4)_2$ nanoparticles from nanorods to nano-spherical particles. Arul et al. [56] prepared $In(OH)_3$ and In_2O_3 micro-powders with a flower-like shape and mesoporous hierarchical microarchitectures by using biuret as an alkaline medium, chelating agent, and surface-anchored organic molecule.

Ceramic powders in the nano-scale range are very useful as functional materials for enhancing the characteristics of materials and as end-use components. Dense compacts of nanoparticles can be shaped to obtain nanoparticles with polydispersed size and uniform shape. Moreover, after thermal treatment under high temperature, the compacts usually exhibit uniform shape and symmetric dimensions, with a dense microstructure (and no detrimental defects) and high mechanical strength. Hu et al. [57] reported that W-Y_2O_3 composite nanopowders with a diameter of 15.1 nm formed W-Y_2O_3 alloys with refined W grains of about 210 nm and a relative density of 98.0%. Insmail et al. [58] implanted TiO_2 nanoflowers on the surface of bauxite-based hollow fiber membranes to enhance their photocatalytic properties under both ultraviolet and visible light.

The zeta potential curves obtained for yttria and thulium-yttria in aqueous solvent are illustrated in Fig. 4. The isoelectric points (IEPs) were recorded for yttria and thulium-yttria at pH 8.2 and pH 8.7, respectively. The zeta potential is zero at the IEP, and thus particles become unstable to form strong agglomerates. Altering the pH of the suspension to far from the IEP is desirable for preparing highly stable suspensions.

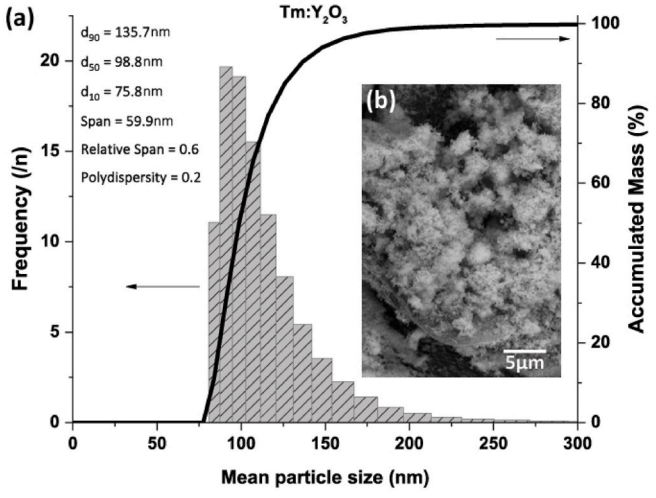

Fig. 3. Particle size and shape characterization for thulium-yttria powders produced using the hydrothermal method, followed by annealing at 1100 °C for 2 h in an air atmosphere: (a) mean particle size distribution determined by photon correlation spectroscopy, and (b) SEM image.

The yttria-based suspensions had significant zeta potential values in the acid pH range (Fig. 4, stage I), but some were not considered given that REs are soluble in the pH range below pH 5.5 according to Sprycha et al. [59]. The stability conditions for the thulium-yttria suspensions were effective except for pH 9.5, and also for yttria except for pH 10.0. In addition, high stability suspensions of yttria and thulium-yttria were obtained at pH 10.5, with ζ values around −31.34 mV and −34.56 mV, respectively (Fig. 4, region IV). Thus, doping with thulium obtained yttria suspensions with a broader range of stability and the dispersion of the particles was enhanced in an aqueous medium.

Previous studies have shown that the characteristics of solvents and additives can affect directly the zeta potentials of particles. Benammar et al. [60] found that the zeta potential of erbium-yttria nanoparticles shifted to 4.5 mV, 10.5 mV, and 48.1 mV in methanol, ethanol, and water, respectively. Hammache et al. [61] showed that the addition of phosphorus-based additives changed the IEP of polymer membranes from pH 4.6 to pH 8.6. Lapo et al. [62] demonstrated that the uptake of REs by adsorption depended directly on the zeta value of the biomaterial, where the ζ-values for banana particles were highly negative at pH 4.5 ($\zeta > -40$ mV) [63], thereby resulting in the maximum adsorption of REs. In a recent study [64] of CeO_2, Eu_2O_3, and Tm_2O_3 based suspensions, the stable conditions promoted by an electrostatic mechanism were established for all of the suspensions in the pH range between 5.5 and 7.5, but not pH 10 ($\zeta > 20$ mV). Another study [65] showed that using polyacrylic acid as a dispersant shifted the IEP of yttria from pH 8.5 to pH 6.6 and provided a broader pH range for preparing stable suspensions.

Colloidal stability is governed by the sum of the potential energies on particles (Vc) corresponding to the following energies: van der Waals (Vw), electrostatic (Ve), steric (Vs), and structural (Vt). Therefore, in order to stabilize colloidal suspensions, the solvent conditions must be adjusted to allow the dispersion of the particles (Fig. 4, regions I and IV). Highly stable concentrated suspensions are desirable for bio-prototyping so they can fill or cover the template in a suitable manner to provide a smooth layer. In addition, stable suspensions allow the formation of powder compacts with uniform shape and size. Considering the results illustrated in Fig. 4 and the aim of preparing highly stable concentrated suspensions for bio-prototyping, the thulium-yttria suspensions were prepared at pH 10.5.

OM images of the thulium-yttria suspensions shaped by bio-prototyping and dried at environmental temperature are shown in Fig. 5. According to Fig. 5a and b, the thulium-yttria suspensions entirely filled the templates to yield a homogeneous mass with no apparent defects such as cracks and bubbles. Furthermore, Fig. 5c and d show that the ceramic suspensions formed a homogenous mass of packed particles after drying at environmental temperature for 24 h. The form of this product was associated with the dispersion of the particles because stable suspensions usually have a uniform arrangement of particles, and thus they also sediment in a uniform manner and adhere strongly to the template's surface. Thus, green powder compacts with a highly packed structure, and regular shape and size were obtained.

Clearly, the stability of the particles in a suspension must be modified by the shaping process. Moreover, changing the stability of particles by adjusting the pH (electrostatic mechanism) may not be sufficient, and thus additives might be required to enhance the dispersion. A recent study [66] showed that the addition of carboxymethyl cellulose changed the pH of yttria suspensions to alkaline, and 0.2 wt% carboxymethyl cellulose was sufficient to yield shear-thinning behavior, which is useful for producing ceramic nettings by bio-prototyping. Marani et al. [67] showed that acidic affine and amphiphilic dispersants were efficient at dispersing gadolinium doped ceria nanoparticles in ethanol to provide suitable concentrated suspensions for tape casting. However, the results obtained in the present study demonstrate that thulium-yttria suspensions can be strongly stabilized without using additives, such as

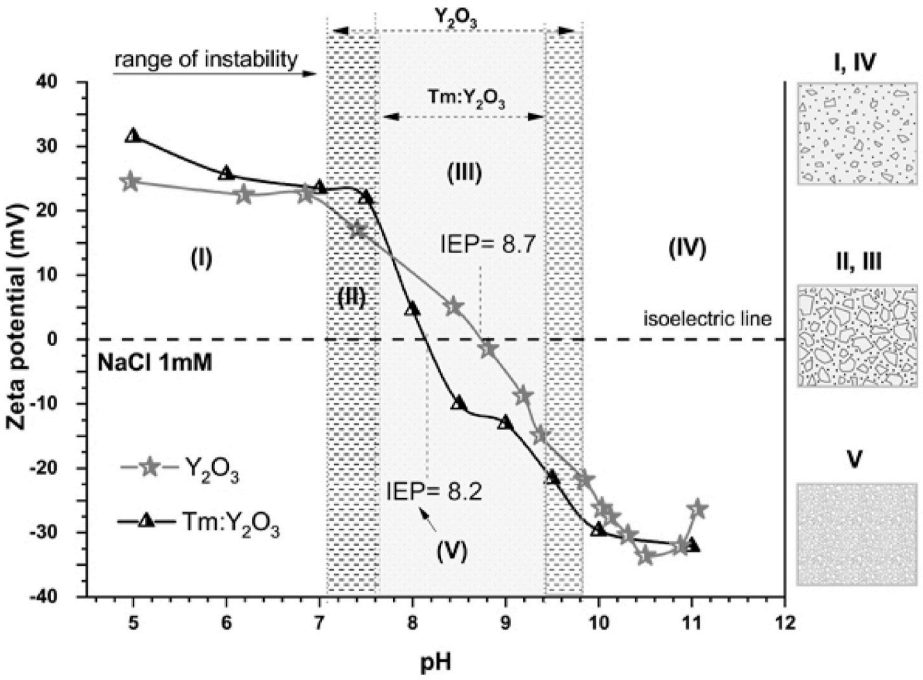

Fig. 4. Zeta potential curves and stabilization stages (from I to V) for yttria and thulium-yttria suspensions as a function of pH.

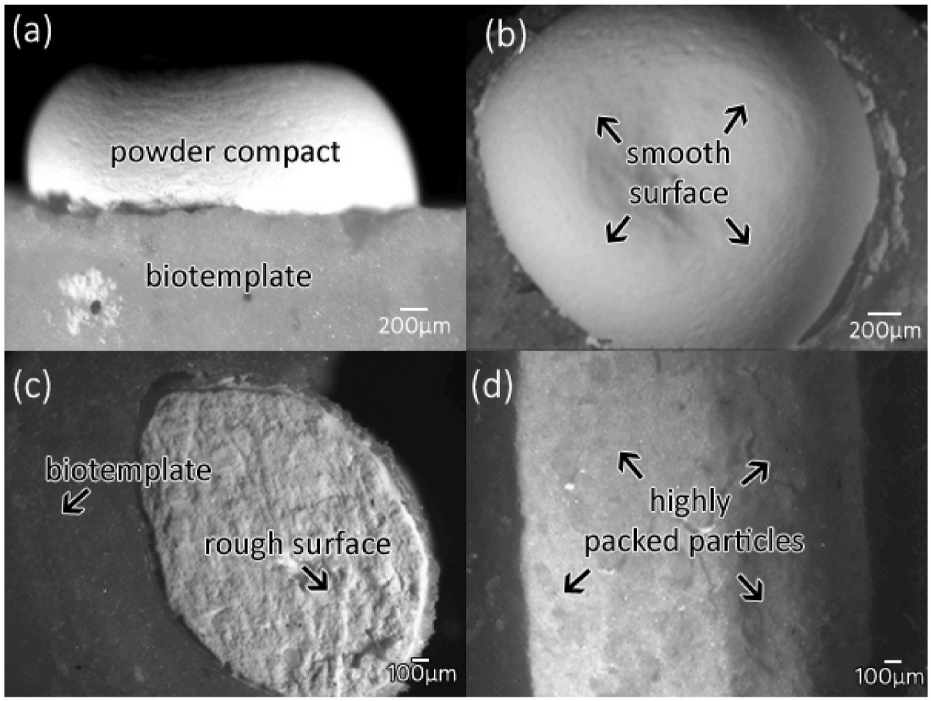

Fig. 5. OM images of a thulium-yttria compact obtained by shaping the ceramic suspension into an organic template, before drying at environmental temperature: (a) top in side view, (b) top, (c) bottom, and (d) left side.

dispersants, surfactants, and binders.

The characteristics of powders and stability of their suspensions greatly affect the packing of particles during shaping. In addition, the thermal treatment conditions directly affect the formation of the microstructure in powder compacts. Bio-prototyping uses organic substances as templates, so it is essential to understand the decomposition behavior of the template as a function of temperature.

In a recent study [68], the vegetable sponge *Luffa cylindrica* was used as a template to produce biomorphic yttria-based ceramics, and *Luffa cylindrica* exhibited the following three distinct decomposition stages according to its constituents and temperature: hemicellulose degradation between 100 and 280 °C, cellulose degradation between 260 and 350 °C, and lignin degradation between 350 and 500 °C. According to a previous evaluation [69], the critical temperature range for the decomposition of the organic template used in the present study is 250–575 °C. Therefore, the heating rate had to be controlled in order to

avoid fragmentation of the sample.

SEM images of a thulium-yttria microceramic sintered at 1600 °C for 2 h under environmental atmosphere are shown in Fig. 6. From a macroscopic perspective (Fig. 6a), the microceramic exhibited uniform size of 3.33 ± 0.01 mm × 2.27 ± 0.01 mm (height × diameter), weight of 62.65 ± 0.02 mg, and no apparent defects. Furthermore, sintering in an air atmosphere yielded samples with a pycnometric density of 4.79 ± 0.01 g cm^{-3}, which corresponds to a relative density of 95.61%. These findings are important because high density yttria samples have been obtained by using sintering aids in a vacuum or hydrogen atmosphere [70–72].

The surface microstructure (Fig. 6b) was relatively dense without cracks, and the grains were bonded at the boundaries to form a triple junction without an unreactive/amorphous phase. The intragranular pores indicated a high rate of grain boundary migration. Chen et al. [73] observed that Zr^{4+} is a powerful grain growth inhibitor in yttria, whereas Sr^{2+} is an effective grain growth promoter. Moreover, according to Fig. 6b, no secondary phases were observed, thereby demonstrating that the thulium-yttria particles were in a solid state after sintering. In addition, microstructural observations confirmed that the thulium-yttria rods were single-phase ceramics.

The fractured surface illustrated in Fig. 6c shows the features of transgranular fractures, with cleavage planes and inner pores, thereby indicating the presence of weak interfaces in the material and pathways for crack propagation across the grains. Cracks continue to grow until they reach a critical length and the remaining uncracked region in the material is no longer able to support the stress applied at the point where complete fracture/failure occurs [74,75].

The densification of ceramics is very important for ceramic processing. Akinc et al. [76] reported that yttria powder compacts should be highly densified (98–99%) at sintering temperatures between 1500 and 1700 °C. Rhodes et al. [77] proposed a method to for limiting grain growth in (La_2O_3-Y_2O_3) based ceramics to obtain pore-free samples by sintering at 2170 °C. Yoshida et al. [78] successfully obtained nearly full-density yttria samples (97.4%) using a flash-sintering approach at a temperature of 985 °C and under an applied DC field of 1000 V cm^{-1}. It was reported that the acceleration of the sintering process is based on the Joule heating of the sample [79].

The microstructural features of ceramic rods depend on the characteristics of the initial powders employed. Thulium-yttria powders comprise acicular particles and the powder compact exhibits four microstructural stages during sintering, as shown in Fig. 7. First, thulium-yttria nanoparticles form junctions in the green body, where high temperature induces a spheroidization process and nanoparticle rearrangement, and thus the powder compact changes to a lower energy state and the number of junctions between the particles increases. Second, coalescence of the nanoparticles occurs, thereby leading to mass transport and a decreased number of void spaces. Third, grain formation and evolution occur due to the densification process. It was reported that no significant temperature difference between the grain boundary and grain interior can be expected in ceramics [80]. Finally, the fourth stage involves grain growth depending on the temperature and time conditions. As shown in Fig. 6b, the grains had different shapes and sizes, thereby suggesting that a higher temperature and time may be have been required to enhance grain growth in the samples. Therefore, the results indicate that the fourth stage of microstructural development was not completed.

The XRD curve obtained for thulium-yttria microceramics sintered at 1600 °C for 2 h under the environmental atmosphere is illustrated in Fig. 8a. The thulium-yttria microceramics (Fig. 8b) exhibited a cubic C-type form (Fig. 8c) with two high intensity peaks at 49.5° and 29.5°, which matched with the (220) plane and (100) plane according to PDF 43-621. In addition, a high intensity peak was recorded at 57.5°, which matched with the (622) plane according to PDF 71-99. As discussed previously and shown in Fig. 2b, the cubic C-type is the most common form of yttria even if it is doped with other REs. This finding is important given that high density yttria has been obtained by using sintering aids in a vacuum or hydrogen atmosphere. In addition, high temperature and pressure are required to induce polymorphisms in yttria, as indicated in Fig. 2c.

RE ions such as Tm^{3+}, Tb^{3+}, Dy^{3+}, and Yb^{3+} are generally used as activators in order to improve the characteristics of the host material, such as the mechanical and chemical strength, and luminescence. Yttria has an intrinsically high number of oxygen vacancies, so it is a very promising potential host material for other RE ions in order to form new dosimetric materials.

The EPR spectra obtained for “pure” yttria and thulium-yttria microceramics are illustrated in Fig. 9a and Fig. 9b, respectively. As shown in our recent study [81], “pure” yttria produced two resonance peaks between 345 and 360 mT, where the main peak p_1 was recorded

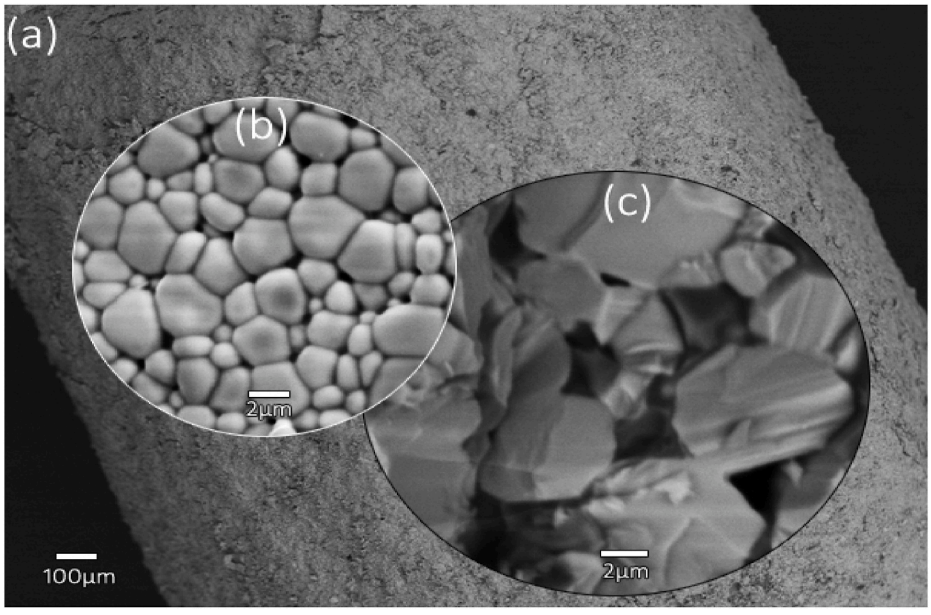

Fig. 6. Thulium-yttria microceramic formed by bio-prototyping, followed by sintering at 1600 °C for 2 h under the environmental atmosphere: (a) macroscopic view, (b) surface microstructure, and (c) inner microstructure with transgranular fractures.

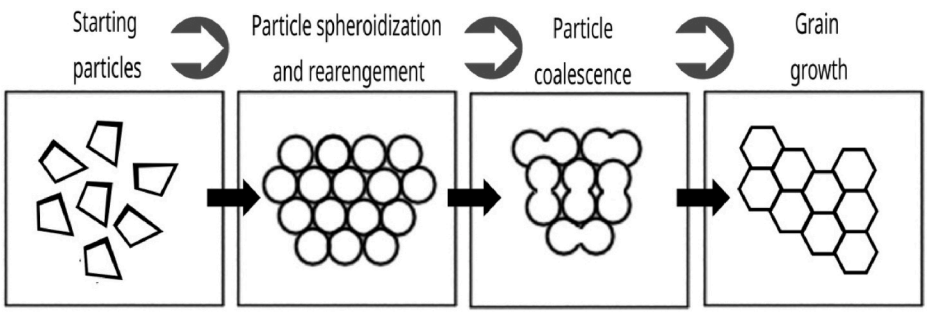

Fig. 7. Formation of the microstructure of thulium-yttria microceramics under sintering at 1600 °C for 2 h in the environmental atmosphere.

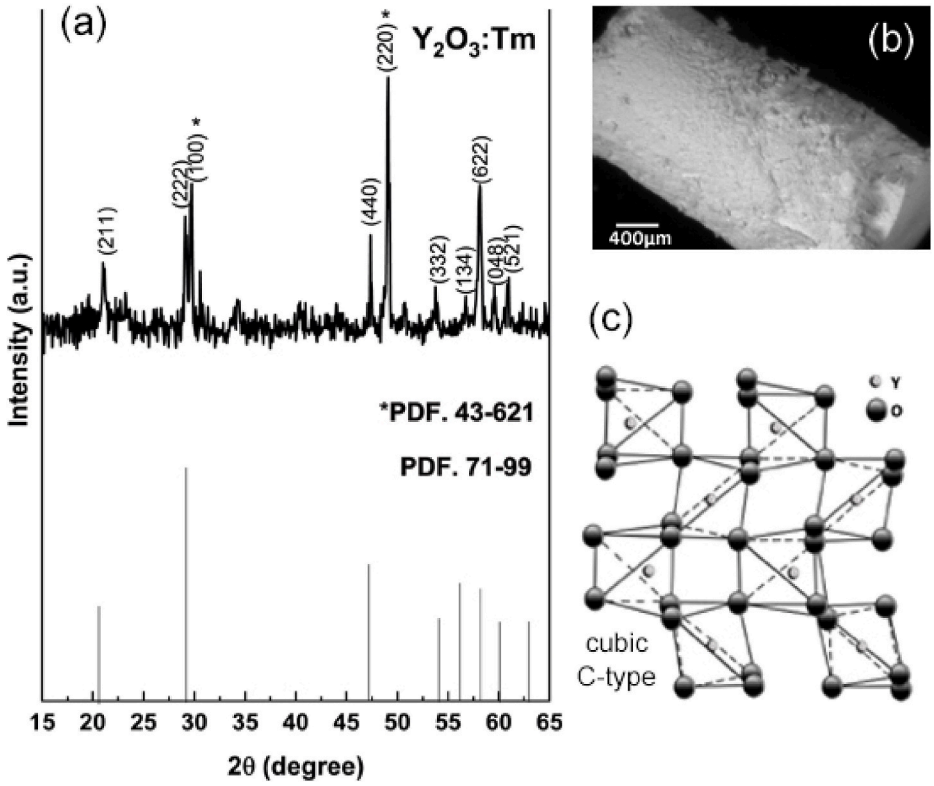

Fig. 8. (a) XRD curve obtained for the as-sintered microceramic. (b) OM image of the microceramic. (c) Spherical model of cubic C-type form.

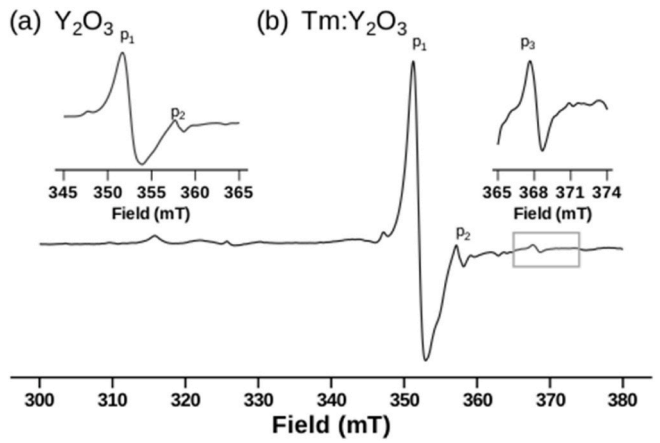

Fig. 9. EPR spectra recorded for microceramics prepared with (a) yttria and (b) thulium-yttria under the environmental atmosphere and temperature.

with g = 2.0000 and a width around 23 G (Fig. 9a). The peak p_1 is associated with the interstitial O^{2-} ion, which is attributable to the adsorption of oxygen from the atmosphere [82]. Osada et al. [83] reported that the O^{2-} ion was recorded at g = 2.040 for samples based on Y_2O_3-CaO. Singh et al. [84] observed the same result for erbium doped yttria (Er:Y_2O_3) where the main peak was recorded at g = 2.0415.

The incorporation of Tm^{3+} into the yttria lattice enhanced the main peak (p_1) response recorded at 351.24 mT, with a line width of 16.8 and g factor of 2.0046 (Fig. 9b). In addition, the p_2 peak recorded at 357.16 mT with a line width of 21.2 and g factor of 1.9714 was associated with the F^+ center, which corresponded to oxygen vacancies containing a remaining electron.

In our recent study of thulium-yttria nanoparticles, thulium-yttria as free powders produced two EPR peaks (p_1 and p_2) recorded at 350 mT and 164 mT, respectively [34]. However, in the present study, the p_2 peaks recorded for the free powders were not present in the spectra obtained for the microceramics, thereby indicating that this defect was not stable at higher temperatures (due to the sintering of microbodies). Previous studies of EPR characterization for REs reported that the formation of radicals in yttria is associated with its lattice characteristics.

Bordun et al. [85] observed that the thermal treatment of yttria under an oxygen atmosphere allowed all of the oxygen vacancies to be filled by oxygen ions from the air atmosphere to yield weak bonds between the new defect centers and intrinsic centers in the lattice. Moreover, in the present study, the incorporation of Tm^{3+} ions led to the development of a new EPR peak assigned to (p_3), which was recorded at 367.64 mT, with a line width of 10.0 and g factor of 1.9162. These results indicate that the peak (p_3) could be ascribed to Tm^{3+} ions integrating in the yttria lattice given that the insertion of Tm^{3+} ions into the yttria lattice occurred by replacing Y^{3+} ions with Tm^{3+} ions in yttria sites C_2 and C_{3i}. Therefore, adding 0.1 at% Tm was useful for producing new charge carriers and it greatly improved the EPR response of yttria.

4. Conclusion

In this study, thulium-yttria microceramics with EPR responses were successfully produced by bio-prototyping. The use of thulium as an activator of yttria enhanced the EPR response by the microceramics, which produced three EPR peaks designated as p_1, p_2, and p_3 with g factors of 2.0046, 1.9714, and 1.9162, respectively. These findings represent further progress in the development of thulium-yttria based materials with potential applications in radiation dosimetry.

Data availability

The raw/processed data required to reproduce these findings cannot be shared at this time due to technical or time limitations.

The raw/processed data required to reproduce these findings cannot be shared at this time as these data also form part of an ongoing study.

Author statement

Santos, S.C: Conceptualization, Methodology, Validation, Formal analysis, Investigation, Writing – original draft, Writing – review & editing, Visualization. Rodrigues, O: Validation, Resources, Data curation, Supervision, Project administration. Campos, L.L: Validation, Resources, Data curation, Supervision, Project administration, Funding acquisition.

Declaration of competing interest

The authors declare that they have no known competing financial interests or personal relationships that could have appeared to influence the work reported in this paper.

Acknowledgments

The authors are very grateful to Dr Maria Elisa Chuery Martins Rostelato of the Radiation Technology Center (CTR) at the Nuclear and Energy Research Institute who kindly allowed us to use the zeta potential analyzer, and Beatriz Ribeiro Nogueira MSc at the same center who helped us with our first use of the equipment. In addition, we acknowledge the following sponsor organizations: São Paulo Research Foundation (FAPESP), National Council for Scientific and Technological Development (CNPq), and Coordination for Improvement of High Degree People (CAPES).

References

[1] M. Esposito, A. Ghirelli, S. Pini, P. Alpi, R. Barca, S. Fondelli, B. Grilli Leonulli, L. Paoletti, F. Rossi, P. Bastiani, S. Russo, Clinical implementation of 3D in vivo dosimetry for abdominal and pelvic stereotactic treatments, Radiother. Oncol. 154 (2021) 14–20, https://doi.org/10.1016/j.radonc.2020.09.011.

[2] M.F. Attallah, H.M. Abdelbary, E.A. Elsofany, Y.T. Mohamed, M.M. Abo-Aly, Radiation safety and environmental impact assessment of sludge TENORM waste produced from petroleum industry in Egypt, Process Saf. Environ. Protect. 142 (2020) 308–316, https://doi.org/10.1016/j.psep.2020.06.012.

[3] K. Hoshi, H. Yoshitomi, K. Aoki, Y. Tanimura, N. Tsujimura, S. Yokoyama, Eye lens dosimetry for workers at Fukushima Daiichi Nuclear Power Plant—1: laboratory study on the dosemeter position and the shielding effect of full face mask respirators, Radiat. Meas. 134 (2020), 106304, https://doi.org/10.1016/j.radmeas.2020.106304.

[4] R.G. Moreira, M.E. Castell-Perez, in: K. Knoerzer, K.B.T.-I.F.P. T. Muthukumarappan (Eds.), 2.01 - Fundamentals of Food Irradiation, Elsevier, Oxford, 2021, pp. 1–18, https://doi.org/10.1016/B978-0-12-815781-7.00008-1.

[5] R. Chen, Chapter 4 - Dose Dependence of Thermoluminescence (TL) and Optically Stimulated Luminescence with Uniform Excitation, Elsevier Science, Amsterdam, 2006, pp. 253–330, https://doi.org/10.1016/B978-044451643-5/50016-2.

[6] L. Bøtter-Jensen, S.W.S. McKeever, A.G. Wintle, Chapter 7 - OSL Measurement Technology, Elsevier, Amsterdam, 2003, pp. 311–350, https://doi.org/10.1016/B978-044450684-9/50094-5.

[7] D.T. Bartlett, 100 years of solid state dosimetry and radiation protection dosimetry, Radiat. Meas. 43 (2008) 133–138, https://doi.org/10.1016/j.radmeas.2007.08.004.

[8] S.B. Almeida, D. Villani, R.K. Sakuraba, A.C.P. Rezende, L.L. Campos, Dosimetric evaluation and comparation of TL responses of LiF:Mg,Ti and μLiF:Mg,Ti in the clinical electron beams dosimetry applied to total skin irradiation (TSEB) treatments, Radiat. Meas. 125 (2019) 15–18, https://doi.org/10.1016/j.radmeas.2019.03.007.

[9] M. Sądel, P. Bilski, M. Kłosowski, M. Sankowska, A new approach to the 2D radiation dosimetry based on optically stimulated luminescence of LiF:Mg,Cu,P, Radiat. Meas. 133 (2020), 106293, https://doi.org/10.1016/j.radmeas.2020.106293.

[10] N. Khalilzadeh, E. Bin Saion, H. Mirabolghasemi, N. Soltani, A.H. Bin Shaari, M. Bin Hashim, N. Mod Ali, A. Dehzangi, Formation and characterization of ultrafine nanophosphors of lithium tetraborate (Li2B4O7) for personnel and medical dosimetry, J. Mater. Res. Technol. 5 (2016) 206–212, https://doi.org/10.1016/j.jmrt.2015.11.002.

[11] F.D.G. Rocha, D. Villani, V.P. Campos, M.S. Nogueira, M.E. Goulart, V.A. Sichito, L. L. Campos, Performance of TL and OSL techniques using CaSO4 and Al2O3 dosimeters for mean glandular dose (MGD) and entrance surface skin dose (ESD) determination in a digital mammographic unit as alternative dosimeters, Radiat, Phys. Chem. 155 (2019) 48–52, https://doi.org/10.1016/j.radphyschem.2018.06.037.

[12] N. Shrestha, E.G. Yukihara, D. Cusumano, L. Placidi, Al2O3:C and Al2O3:C,Mg optically stimulated luminescence 2D dosimetry applied to magnetic resonance guided radiotherapy, Radiat. Meas. 138 (2020), 106439, https://doi.org/10.1016/j.radmeas.2020.106439.

[13] M.S. Bhadane, K. Hareesh, S.S. Dahiwale, K.R. Sature, B.J. Patil, K. Asokan, D. Kanjilal, V.N. Bhoraskar, S.D. Dhole, A highly sensitive CaF2:Dy nanophosphor as an efficient low energy ion dosimetry, Nucl. Instrum. Methods Phys. Res. Sect. B Beam Interact. Mater. Atoms 386 (2016) 61–69, https://doi.org/10.1016/j.nimb.2016.09.017.

[14] S.C. Santos, C. Yamagata, L.L. Campos, S.R.H. Mello-Castanho, Processing and thermoluminescent response of porous biomorphic dysprosium doped yttrium disilicate burner, Mater. Chem. Phys. 177 (2016) 505–511, https://doi.org/10.1016/j.matchemphys.2016.04.061.

[15] S.C. Santos, W. Acchar, C. Yamagata, S. Mello-Castanho, Yttria nettings by colloidal processing, J. Eur. Ceram. Soc. 34 (2014) 2509–2517, https://doi.org/10.1016/j.jeurceramsoc.2014.03.006.

[16] S.C. Santos, C. Yamagata, A.C. Silva, L.F.G. Setz, S.R.H. Mello-Castanho, Yttrium disilicate micro-cellular architecture from biotemplating of Luffa Cylindrica, J. Ceram. Sci. Technol. 5 (2014) 203–208, https://doi.org/10.4416/JCST2014-00008.

[17] S.C. Santos, O. Rodrigues, L.L. Campos, EPR response of yttria micro rods activated by europium, J. Alloys Compd. (2018), https://doi.org/10.1016/j.jallcom.2018.06.063.

[18] B. Aksakal, M. Demirel, The effect of Zirconia/Yttria/Silver substitutions on mechanostructure and cell viability of the synthesized bioceramic bone grafts, Ceram. Int. 43 (2017) 7482–7487, https://doi.org/10.1016/j.ceramint.2017.03.026.

[19] M.H. Shaaban, A.A. Ali, Density, electrical and optical properties of yttrium-containing tellurium bismuth borate glasses, J. Electron. Mater. 43 (2014) 4023–4032, https://doi.org/10.1007/s11664-014-3331-y.

[20] Y.K. Kim, H.K. Kim, G. Cho, D.K. Kim, Effect of yttria substitution on the light output of (Gd,Y)2O3:Eu ceramic scintillator, Nucl. Instrum. Methods Phys. Res. Sect. B Beam Interact. Mater. Atoms 225 (2004) 392–396, https://doi.org/10.1016/j.nimb.2004.03.087.

[21] C. Liao, X. Zou, C.W. Huang, J. Wang, K. Zhang, Y. Kong, T. Chen, W.W. Wu, X. Xiao, C. Jiang, L. Liao, Low interface trap densities and enhanced performance of AlGaN/GaN MOS high- electron mobility transistors using thermal oxidized Y_2O_3 interlayer, IEEE Electron. Device Lett. 36 (2015) 1284–1286, https://doi.org/10.1109/LED.2015.2486818.

[22] F. Hayashi, M. Tanaka, D. Lin, M. Iwamoto, Surface structure of yttrium-modified ceria catalysts and reaction pathways from ethanol to propene, J. Catal. 316 (2014) 112–120, https://doi.org/10.1016/j.jcat.2014.04.017.

[23] T. Mongstad, A. Thogersen, A. Subrahmanyam, S. Karazhanov, The electronic state of thin films of yttrium, yttrium hydrides and yttrium oxide, Sol. Energy Mater. Sol. Cells 128 (2014) 270–274, https://doi.org/10.1016/j.solmat.2014.05.037.

[24] A. Kruk, A. Wajler, M. Bobruk, A. Adamczyk, M. Mrózek, W. Gawlik, T. Brylewski, Preparation of yttria powders co-doped with Nd3+, and La3+ using EDTA gel processes for application in transparent ceramics, J. Eur. Ceram. Soc. 37 (2017) 4129–4140, https://doi.org/10.1016/j.jeurceramsoc.2017.05.040.

[25] L. Gan, Y.-J. Park, L.-L. Zhu, H.-N. Kim, J.-W. Ko, J.-W. Lee, Highly transparent Nd-doped yttria ceramics fabricated by hot pressing with ZrO2 and La2O3 as sintering additives, J. Alloys Compd. 763 (2018) 192–198, https://doi.org/10.1016/j.jallcom.2018.05.304.

[26] A divalent rare earth oxide semiconductor: yttrium monoxide, Appl. Phys. Lett. 108 (2016), 122102, https://doi.org/10.1063/1.4944330.

[27] R. Praveena, K. Balasubrahmanyam, L. Jyothi, G. Venkataiah, C. K. Basavapoornima, C.K. Jayasankar, White light generation from Dy3+-doped yttrium aluminium gallium mixed garnet nano-powders, J. Lumin. 170 (2016) 262–270, https://doi.org/10.1016/j.jlumin.2015.10.012.

[28] L. Zhang, D.Y. Jiang, J.F. Xia, C.X. Li, N. Zhang, Q. Li, Novel luminescent yttrium oxide nanosheets doped with Eu3+ and Tb3+, RSC Adv. 4 (2014) 17648–17652, https://doi.org/10.1039/C4ra01881h.

[29] N.A. Oliveira, A.G. Bispo Jr., G.M.M. Shinohara, S.A.M. Lima, A.M. Pires, The influence of the complexing agent on the luminescence of multicolor-emitting Y2O3:Eu3+,Er3+,Yb3+ phosphors obtained by the Pechini's method, Mater. Chem. Phys. 257 (2021), 123840, https://doi.org/10.1016/j.matchemphys.2020.123840.

[30] G. Yuan, M. Li, M. Yu, C. Tian, G. Wang, H. Fu, In situ synthesis, enhanced luminescence and application in dye sensitized solar cells of Y2O3/Y2O2S:Eu3+ nanocomposites by reduction of Y2O3:Eu3+, Sci. Rep. 6 (2016), 37133 https://doi.org/10.1038/srep37133.

[31] E.F. Huerta, J. De Anda, I. Martínez-Merlin, U. Caldiño, C. Falcony, Near-infrared luminescence spectroscopy in yttrium oxide phosphor activated with Er3+, Li+ and Yb3+ ions for application in photovoltaic systems, J. Lumin. 224 (2020), 117271, https://doi.org/10.1016/j.jlumin.2020.117271.

[32] M. Fabrice, A. Fulvio, B. Silvia, N. Philip, B. Giovanni, A.D. Patricia, B. Darina, T.D. M. Cristina, W. Dominic, P. Claudiu, H. Tamas, S. Hans, G. Bernd, O. Glenn, H. Dries, G. Elena, T. Evangelos, B. Faycal, S. Slavko, Critical Raw Materials and the Circular Economy – Background Report, 2017, https://doi.org/10.2760/378123.

[33] U.S.G.S. Department of the Interior, U.S.G.S. Department of the Interior, U.S.G.S. Department of the Interior, A Federal Strategy to Ensure Secure and Reliable Supplies of Critical Minerals, 2018. United States, https://www.usgs.gov/news/interior-releases-2018-s-final-list-35-minerals-deemed-critical-us-national-security-and.

[34] S.C. Santos, Ot. a new promising dosimetric material from formation of thulium-yttria nanoparticles with E. response Rodrigues, L.L. Campos, towards a new promising dosimetric material from formation of thulium-yttria nanoparticles with EPR response, Mater. Chem. Phys. 259 (2021), 124005, https://doi.org/10.1016/j.matchemphys.2020.124005.

[35] S.C. Santos, Ot. a new promising dosimetric material from formation of thulium-yttria nanoparticles with E. response Rodrigues, L.L. Campos, towards a new promising dosimetric material from formation of thulium-yttria nanoparticles with EPR response, Mater. Chem. Phys. 259 (2021), 124005, https://doi.org/10.1016/j.matchemphys.2020.124005.

[36] R. Moreno, in: Reología de suspensiones cerámicas, first ed., Consejo Superior de Investigaciones Científicas, Spain, 2005.

[37] D.N. Thomas, S.J. Judd, N. Fawcett, Flocculation modelling: a review, Water Res. 33 (1999) 1579–1592, https://doi.org/10.1016/S0043-1354(98)00392-3.

[38] A. Govindasamy, C. Lv, H. Tsuboi, M. Koyama, A. Endou, M. Kubo, E. Broclawik, A. Miyamoto, A theoretical study of the effect of Eu ion dopant on the electronic excitations of yttrium oxide and yttrium oxy-sulphide, Japanese J. Appl. Phys. Part 1-Regular Pap, Br. Commun. Rev. Pap. 45 (2006) 5782–5785, https://doi.org/10.1143/Jjap.45.5782.

[39] Silas Cardoso Santos, Orlando Rodrigues Junior, Leticia Lucente Campos, Advances in colloidal processing of rare earth particles, Curr. Smart Mater. (2017), https://doi.org/10.2174/2405465802666171012143956.

[40] Y.N. Xu, Z.Q. Gu, W.Y. Ching, Electronic, structural, and optical properties of crystalline yttria, Phys. Rev. B 56 (1997) 14993–15000. https://link.aps.org/doi/10.1103/PhysRevB.56.14993.

[41] T.-J. Wang, F.-X. Hua, Y.-H. Chang, G.-L. Peng, M.-H. Chou, W.-K. Hung, Effects of erbium content on the morphological and photoluminescent properties of sol-gel prepared yttrium oxide film, Ceram. Int. 44 (2018) 1916–1921, https://doi.org/10.1016/j.ceramint.2017.10.132.

[42] T. Verma, S. Agrawal, Optical studies and estimation of kinetic parameters for dysprosium activated yttrium oxide phosphors, Optik 160 (2018) 361–370, https://doi.org/10.1016/j.ijleo.2018.02.015.

[43] D.A. Permin, S. V Kurashkin, A. V Novikova, A.P. Savikin, E.M. Gavrishchuk, S. S. Balabanov, N.M. Khamaletdinova, Synthesis and luminescence properties of Yb-doped Y2O3, Sc2O3 and Lu2O3 solid solutions nanopowders, Opt. Mater. 77 (2018) 240–245, https://doi.org/10.1016/j.optmat.2018.01.041.

[44] D.T. Cromer, The crystal structure of monoclinic Sm202, J. Phys. Chem. 61 (1957) 753–755, https://doi.org/10.1021/j150552a011.

[45] R.M. Douglass, E. Staritzky, Crystallographic data. 112. Samarium sesquioxide, Sm2O3, form B, Anal. Chem. 28 (1956) 552, https://doi.org/10.1021/ac50161a049.

[46] M.D.Z.K. Pauling, L. Shappell, The crystal structure of bixbyite and the C-modification of the sesquioxides, Z. Kristallogr. 75 (1930) 128–142. https://chemport.cas.org/cgi-bin/sdcgi?APP=ftslink&action=reflink&origin=ACS&version=1.0&coi=1%3ACAS%3A528%3ADyaA3MXhtlagsw%253D%253D&md5=b026f03d788c70076a3439bae1724027.

[47] M. Foex, Allotropic transformations of rare earth sesquioxides, J. Inorg. Gen. Chem. ZAAC. 337 (1965) 313–324, https://doi.org/10.1002/zaac.19653370511.

[48] G. Brauer, Progress in the Science and Technology of the Rare Earths, Pergamon Press, Oxford, 1966. https://scholar.google.com/scholar_lookup?hl=en&publication_year=1966&pages=312&author=G.+Brauer&title=Progress+in+the+Science+and+Technology+of+the+Rare+Earths.

[49] P. Aldebert, J.P. Traverse, Neutron diffraction study of high temperature structures of La2O3 and Nd2O3, Mater. Res. Bull. 14 (1979) 303–323, https://doi.org/10.1016/0025-5408(79)90095-3.

[50] H.R. Hoekstra, K.A. Gingerich, High-pressure B-type polymorphs of some rare-earth sesquioxides, Science (80-.) 146 (1964) 1163–1164, https://doi.org/10.1126/science.146.3648.1163.

[51] V. Gourlaouen, G. Schnedecker, A.M. Lejus, M. Boncoeur, R. Collongues, Metastable phases in yttrium oxide plasma spray deposits and their effect on coating properties, Mater. Res. Bull. 28 (1993) 415–425, https://doi.org/10.1016/0025-5408(93)90123-U.

[52] H. Starr, Territory, proximity, and spatiality: the geography of international conflict, Int. Stud. Rev. 7 (2005) 387–406, https://doi.org/10.1111/j.1551-2916.2005.00506.x.

[53] X. Qin, Y. Ju, S. Bernhard, N. Yao, Flame synthesis of Y 2 O 3 :Eu nanophosphors using ethanol as precursor solvents, J. Mater. Res. 20 (2005) 2960–2968, https://doi.org/10.1557/JMR.2005.0364.

[54] S.C. Santos, O. Rodrigues, L.L. Campos, Synthesis, processing and electron paramagnetic resonance response of Y1.98Eu0.02O3 micro rods, Int. J. Mod. Phys. Conf. Ser. 48 (2018), 1860112, https://doi.org/10.1142/S2010194518601126.

[55] X. Yu, Z. Han, H. Tang, J. Xie, X. Mi, Investigating luminescence properties and energy transfer of Ca3(PO4)2: Dy3+/Eu3+ phosphor via hydrothermal synthesis, Opt. Mater. 106 (2020), 110009, https://doi.org/10.1016/j.optmat.2020.110009.

[56] B. Arul Prakasam, M. Lahtinen, A. Peuronen, M. Muruganandham, M. Sillanpää, Facile fabrication of flower like self-assembled mesoporous hierarchical microarchitectures of In(OH)3 and In2O3: in(OH)3 micro flowers with electron beam sensitive thin petals, Mater. Chem. Phys. 184 (2016) 183–188, https://doi.org/10.1016/j.matchemphys.2016.09.040.

[57] W. Hu, Z. Dong, Z. Ma, Y. Liu, W–Y2O3 composite nanopowders prepared by hydrothermal synthesis method: Co-deposition mechanism and low temperature sintering characteristics, J. Alloys Compd. 821 (2020), 153461, https://doi.org/10.1016/j.jallcom.2019.153461.

[58] N.J. Ismail, M.H.D. Othman, S. Abu Bakar, S.H. Sheikh Abdul Kadir, M.H. Abd Aziz, M.A.B. Pauzan, S.K. Hubadillah, T. El-badawy, J. Jaafar, M. A Rahman, Hydrothermal synthesis of TiO2 nanoflower deposited on bauxite hollow fibre membrane for boosting photocatalysis of bisphenol A, J. Water Process Eng. 37 (2020), 101504, https://doi.org/10.1016/j.jwpe.2020.101504.

[59] J.J. Ryszard, Sprycha egon Matijevic, zeta potential and surface charge of monodispersed colloidal yttrium (III) oxide and basic carbonate, J. Colloid Interface Sci. 149 (1991) 562–568, https://doi.org/10.1016/0021-9797(92)90443-P.

[60] I. Benammar, R. Salhi, J.-L. Deschanvres, R. Maalej, The effect of rare earth element (Er, Yb) doping and heat treatment on suspension stability of Y2O3 nanoparticles elaborated by sol-gel method, J. Mater. Res. Technol. 9 (2020) 12634–12642, https://doi.org/10.1016/j.jmrt.2020.08.105.

[61] Z. Hammache, S. Bensaadi, Y. Berbar, N. Audebrand, A. Szymczyk, M. Amara, Recovery of rare earth elements from electronic waste by diffusion dialysis, Separ. Purif. Technol. 254 (2021), 117641, https://doi.org/10.1016/j.seppur.2020.117641.

[62] B. Lapo, J.J. Bou, J. Hoyo, M. Carrillo, K. Peña, T. Tzanov, A.M. Sastre, A potential lignocellulosic biomass based on banana waste for critical rare earths recovery from aqueous solutions, Environ. Pollut. 264 (2020), 114409, https://doi.org/10.1016/j.envpol.2020.114409.

[63] R.D. Harding, Heterocoagulation in mixed dispersions—effect of particle size, size ratio, relative concentration, and surface potential of colloidal components, J. Colloid Interface Sci. 40 (1972) 164–173, https://doi.org/10.1016/0021-9797(72)90006-9.

[64] S. Santos, O. Rodrigues, L. Campos, A Glance on Rare Earth Oxides : Importance , Reserves , Demand , Applications , Critical Uncertainties , Global Economy , and Zeta Potential Characterization, 2020, pp. 1–22, https://doi.org/10.2174/2405465805999200628095450.

[65] S.C. Santos, C. Yamagata, W. Acchar, S.R.H. Mello-Castanho, Yttria Nettings by Replica Processing, 2014. https://doi.org/10.4028/www.scientific.net/MSF.798-799.687.

[66] S.C. Santos, C. Yamagata, L.L. Campos, S.R.H. Mello-Castanho, Processing, microstructure and thermoluminescence response of biomorphic yttrium oxide ceramics, Ceram. Int. (2016), https://doi.org/10.1016/j.ceramint.2016.05.136.

[67] D. Marani, B.R. Sudireddy, J.J. Bentzen, P.S. Jørgensen, R. Kiebach, Colloidal stabilization of cerium-gadolinium oxide (CGO) suspensions via rheology, J. Eur. Ceram. Soc. 35 (2015) 2823–2832, https://doi.org/10.1016/j.jeurceramsoc.2015.03.043.

[68] S.C. Santos, C. Yamagata, L.L. Campos, S.R.H. Mello-Castanho, Bio-prototyping and thermoluminescence response of cellular rare earth ceramics, J. Eur. Ceram. Soc. 36 (2016) 791–796, https://doi.org/10.1016/j.jeurceramsoc.2015.10.024.

[69] S.C. Santos, O. Rodrigues, L.L. Campos, Bio-prototyping of europium-yttria based rods for radiation dosimetry, Mater. Chem. Phys. (2017), https://doi.org/10.1016/j.matchemphys.2017.07.063.

[70] R.A. Lefever, J. Matsko, Transparent yttrium oxide ceramics, Mater. Res. Bull. 2 (1967) 865–869, https://doi.org/10.1016/0025-5408(67)90096-7.

[71] Y. Huang, D. Jiang, J. Zhang, Q. Lin, Fabrication of transparent lanthanum-doped yttria ceramics by combination of two-step sintering and vacuum sintering, J. Am. Ceram. Soc. 92 (2009) 2883–2887, https://doi.org/10.1111/j.1551-2916.2009.03312.x.

[72] T. Ikegami, J.-G. Li, T. Mori, Y. Moriyoshi, Fabrication of transparent yttria ceramics by the low-temperature synthesis of yttrium hydroxide, J. Am. Ceram. Soc. 85 (2002) 1725–1729, https://doi.org/10.1111/j.1151-2916.2002.tb00342.x.
[73] P.-L. Grain, Boundary mobility in Y2O3: defect mechanism and dopant Effects Chen, I.-W. Chen, grain boundary mobility in Y2O3: defect mechanism and dopant effects, J. Am. Ceram. Soc. 79 (1996) 1801–1809, https://doi.org/10.1111/j.1151-2916.1996.tb07998.x.
[74] A. Mouritz (Ed.), 18 - Fracture Processes of Aerospace Materials, Woodhead Publishing, 2012, pp. 428–453, https://doi.org/10.1533/9780857095152.428.
[75] M. Anglada, in: P. Palmero, E. De Barra, F. Cambier (Eds.), 3 - Assessment of Mechanical Properties of Ceramic Materials, Woodhead Publishing, 2017, pp. 83–109, https://doi.org/10.1016/B978-0-08-100881-2.00003-8.
[76] D.J. Sordelet, M. Akinc, Sintering of monosized, spherical yttria powders, J. Am. Ceram. Soc. 71 (1988) 1148–1153, https://doi.org/10.1111/j.1151-2916.1988.tb05807.x.
[77] W.H. Rhodes, Controlled transient solid second-phase sintering of yttria, J. Am. Ceram. Soc. 64 (1981) 13–19, https://doi.org/10.1111/j.1151-2916.1981.tb09551.x.
[78] H. Yoshida, Y. Sakka, T. Yamamoto, J.-M. Lebrun, R. Raj, Densification behaviour and microstructural development in undoped yttria prepared by flash-sintering, J. Eur. Ceram. Soc. 34 (2014) 991–1000, https://doi.org/10.1016/j.jeurceramsoc.2013.10.031.
[79] R. Raj, Joule heating during flash-sintering, J. Eur. Ceram. Soc. 32 (2012) 2293–2301, https://doi.org/10.1016/j.jeurceramsoc.2012.02.030.
[80] T.B. Holland, U. Anselmi-Tamburini, D. V Quach, T.B. Tran, A.K. Mukherjee, Effects of local Joule heating during the field assisted sintering of ionic ceramics, J. Eur. Ceram. Soc. 32 (2012) 3667–3674, https://doi.org/10.1016/j.jeurceramsoc.2012.02.033.
[81] S.C. Santos, O. Rodrigues, L.L. Campos, EPR dosimetry of yttria micro rods, J. Alloys Compd. (2018), https://doi.org/10.1016/j.jallcom.2018.01.315.
[82] J.H. Lunsford, Esr of adsorbed oxygen species, Catal. Rev. Eng. 8 (1973) 135–157.
[83] Y. Osada, S. Koike, T. Fukushima, S. Ogasawara, T. Shikada, T. Ikariya, Oxidative coupling of methane over Y2o3-cao catalysts, Appl. Catal. 59 (1990) 59–74, https://doi.org/10.1016/S0166-9834(00)82187-9.
[84] K. Singh, V. Thangadurai, Chemical reactivity between Ce0.7RE0.2Mo0.1O2 (RE = Y, Sm) and 8YSZ, and conductivity studies of their solid solutions, Solid State Ionics 262 (2014) 444–448, https://doi.org/10.1016/j.ssi.2014.03.030.
[85] O.M. Bordun, Influence of oxygen vacancies on the luminescence spectra of Y2O3 thin films, J. Appl. Spectrosc. 69 (2002) 430–433, https://doi.org/10.1023/a:1019763518857.